

# Towards human SuperEEG

Lucy L. W. Owen<sup>1</sup>, Andrew C. Heusser<sup>1,2</sup>, and Jeremy R. Manning<sup>1\*</sup>

<sup>1</sup>Department of Psychological and Brain Sciences, Dartmouth College,  
Hanover, NH 03755, USA

<sup>2</sup>Akili Interactive,  
Boston, MA 02110, USA

## Abstract

Human *SuperEEG*<sup>1</sup> entails measuring ongoing neural activity with perfect precision and at arbitrarily high spatiotemporal resolution. Although true SuperEEG is impossible using existing methods, here we present a model-based method for *inferring* neural activity at millimeter-scale spatial resolutions and millisecond-scale temporal resolutions using standard human intracranial recordings. Our approach assumes that different people's brains exhibit similar spatial correlations, and that (all else being equal) neural activity at nearby locations will tend to be similar. One can then ask, for an arbitrary individual's brain: given recordings from a limited set of locations in that individual's brain, along with the observed spatial correlations learned from other people's recordings, how much can be inferred about ongoing activity at *other* locations in that individual's brain?

**Keywords:** Electrocorticography (ECoG), intracranial electroencephalography (iEEG), local field potential (LFP), epilepsy, maximum likelihood estimation, Gaussian process regression

## Introduction

Modern human brain recording techniques are fraught with compromise [33]. Commonly used approaches include functional magnetic resonance imaging (fMRI), scalp electroencephalography (EEG), and magnetoencephalography (MEG). For each of these techniques, neuroscientists and electrophysiologists must choose to optimize spatial resolution at the cost of temporal resolution (e.g., as in fMRI) or temporal resolution at the cost of spatial resolution (e.g., as in EEG and MEG). A less widely used approach (due to requiring work with neurosurgical patients) is to record from electrodes implanted directly onto the cortical surface (electrocorticography; ECoG)

---

<sup>1</sup>The term "SuperEEG" was coined by Robert J. Sawyer in his popular science fiction novel *The Terminal Experiment* [29]

25 or into deep brain structures (intracranial EEG; iEEG). However, these intracranial approaches  
26 also require compromise: the high spatiotemporal resolutions of intracranial recordings comes  
27 at the cost of substantially reduced brain coverage, since safety considerations limit the number  
28 of electrodes one may implant in a given patient’s brain. Further, the locations of implanted  
29 electrodes are determined by clinical, rather than research, needs.

30 An increasingly popular approach is to improve the effective spatial resolution of MEG or  
31 scalp EEG data by using a geometric approach called *beamforming* to solve the biomagnetic or  
32 bioelectrical inverse problem [28]. This approach entails using detailed brain conductance mod-  
33 els (often informed by high spatial resolution anatomical MRI images) along with the known  
34 sensor placements (localized precisely in 3D space) to reconstruct brain signals originating from  
35 theoretical point sources deep in the brain (and far from the sensors). Traditional beamforming  
36 approaches must overcome two obstacles. First, the inverse problem beamforming seeks to  
37 solve has infinitely many solutions. Researchers have made traction towards constraining the  
38 solution space by assuming that signal-generating sources are localized on a regularly spaced  
39 grid spanning the brain and that individual sources are small relative to their distances to the  
40 sensors [1, 11, 34]. The second, and in some ways much more serious, obstacle is that the  
41 magnetic fields produced by external (noise) sources are substantially stronger than those pro-  
42 duced by the neuronal changes being sought (i.e., at deep structures, as measured by sensors  
43 at the scalp). This means that obtaining adequate signal quality often requires averaging the  
44 measured responses over tens to hundreds of responses or trials (e.g., see review by [11]).

45 Another approach to obtaining high spatiotemporal resolution neural data has been to col-  
46 lect fMRI and EEG data simultaneously. Simultaneous fMRI-EEG has the potential to balance  
47 the high spatial resolution of fMRI with the high temporal resolution of scalp EEG, thereby,  
48 in theory, providing the best of both worlds. In practice, however, the signal quality of both  
49 recordings suffers substantially when the two techniques are applied simultaneously (e.g., see

50 review by [13]). In addition, the experimental designs that are ideally suited to each technique  
51 individually are somewhat at odds. For example, fMRI experiments often lock stimulus presen-  
52 tation events to the regularly spaced image acquisition time (TR), which maximizes the number  
53 of post-stimulus samples. By contrast, EEG experiments typically employ jittered stimulus pre-  
54 sentation times to maximize the experimentalist’s ability to distinguish electrical brain activity  
55 from external noise sources such as from 60 Hz alternating current power sources.

56 The current “gold standard” for precisely localizing signals and sampling at high temporal  
57 resolution is to take (ECoG or iEEG) recordings from implanted electrodes (but from a limited  
58 set of locations in any given brain). This begs the following question: what can we infer  
59 about the activity exhibited by the rest of a person’s brain, given what we learn from the  
60 limited intracranial recordings we have from their brain and additional recordings taken from  
61 *other* people’s brains? Here we develop an approach, which we call *SuperEEG*, based on  
62 Gaussian process regression [27]. SuperEEG entails using data from multiple people to estimate  
63 activity patterns at arbitrary locations in each person’s brain (i.e., independent of their electrode  
64 placements). We test SuperEEG approach using two large datasets of intracranial recordings [7,  
65 8, 12, 16–19, 21, 23, 30–32, 35, 40]. We show that the SuperEEG algorithm recovers signals well  
66 from electrodes that were held out of the training dataset. We also examine the factors that  
67 influence how accurately activity may be estimated (recovered), which may have important  
68 implications for electrode design and placement in neurosurgical applications.

## 69 Approach

70 The SuperEEG approach to inferring high temporal resolution full-brain activity patterns is  
71 outlined and summarized in Figure 1. We describe (in this section) and evaluate (in *Results*) our  
72 approach using a two large previously collected dataset comprising multi-session intracranial  
73 recordings. Dataset 1 comprises multi-session recordings taken from 6876 electrodes implanted

74 in the brains of 88 epilepsy patients [21, 23, 30–32]. Each recording session lasted from 0.2–3.0  
75 (total recording time: 0.3–14.2 hours; Fig. S4A), and includes data from a list-learning memory  
76 experiment for up to one hour varying by patient with additional buffer time in which the  
77 patients performed typical bed-ridden hospital activities. For the purposes of the Dataset  
78 1 analyses presented here, we aggregated all data across each recording session, ignoring the  
79 particular activities or tasks the patients were performing at any given moment. We used Dataset  
80 1 to develop our main SuperEEG approach, and to examine the extent to which SuperEEG might  
81 be able to generate task-general predictions. Dataset 2 comprised multi-session recordings from  
82 4436 electrodes implanted in the brains of 40 epilepsy patients [7, 8, 12, 16–19, 35, 40]. Each  
83 recording session lasted from 0.4–2.2 hours (total recording time: 0.4–6.6 hours; Fig. S4B).  
84 Whereas Dataset 1 included recordings taken during a wide variety of behaviors, Dataset 2  
85 included recordings taken as each patient performed each of two memory tasks: a random  
86 word list free recall task and a categorized word list free recall task. We used Dataset 2 to  
87 further examine the ability of SuperEEG to generalize its predictions within versus across tasks.  
88 Figure S4 provides additional details on both datasets.

89 We first applied fourth order Butterworth notch filter to remove 60 Hz ( $\pm .5$  Hz) line noise  
90 from every recording (from every electrode). Next, we downsampled the recordings (regardless  
91 of the original samplerate) to 250 Hz. (This downsampling step served to both normalize for  
92 differences in sampling rates across patients and to ease the computational burden of our sub-  
93 sequent analyses.) We then excluded any electrodes that showed putative epileptiform activity.  
94 Specifically, we excluded from further analysis any electrode that exhibited an average kurtosis  
95 of 10 or greater across all of that patient’s recording sessions. We also excluded any patients  
96 with fewer than 2 electrodes that passed this criteria, as the SuperEEG algorithm requires  
97 measuring correlations between 2 or more electrodes from each patient. For Dataset 1, this  
98 yielded clean recordings from 4168 electrodes implanted throughout the brains of 67 patients

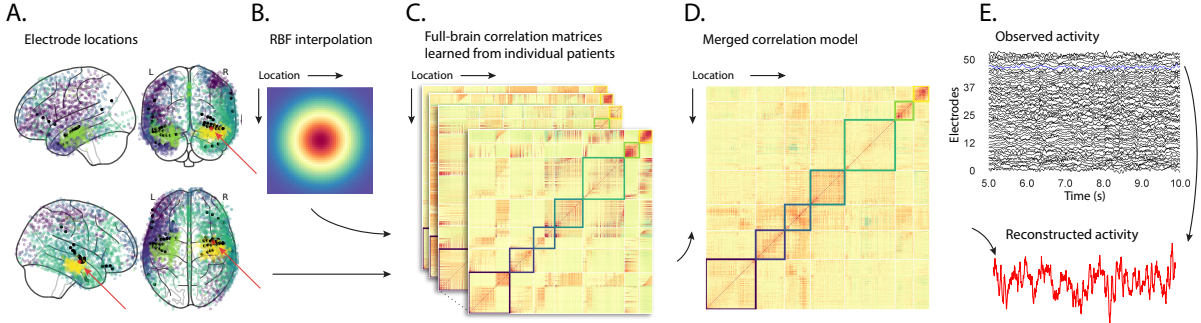


**Figure 1: Methods overview.** **A. Electrode locations.** Each dot reflects the location of a single electrode implanted in the brain of a Dataset 1 patient. A held-out recording location from one patient is indicated in red, and the patient’s remaining electrodes are indicated in black. The electrodes from the remaining patients are colored by  $k$ -means cluster (computed using the full-brain correlation model shown in Panel D). **B. Radial basis function kernel.** Each electrode contributed by the patient (black) weights on the full set of locations under consideration (all dots in Panel A, defined as  $\bar{R}$  in the text). The weights fall off with positional distance (in MNI space) according to an RBF. **C. Per-patient correlation matrices.** After computing the pairwise correlations between the recordings from each patient’s electrodes, we use RBF-weighted averages to estimate correlations between all locations in  $\bar{R}$ . We obtain an estimated full-brain correlation matrix using each patient’s data. **D. Merged correlation model.** We combine the per-patient correlation matrices (Panel C) to obtain a single full-brain correlation model that captures information contributed by every patient. Here we have sorted the rows and columns to reflect  $k$ -means clustering labels [using  $k=7; 41$ ], whereby we grouped locations based on their correlations with the rest of the brain (i.e., rows of the matrix displayed in the panel). The boundaries denote the cluster groups. The rows and columns of Panel C have been sorted using the Panel D-derived cluster labels. **E. Reconstructing activity throughout the brain.** Given the observed recordings from the given patient (shown in black; held-out recording is shown in blue), along with a full-brain correlation model (Panel D), we use Equation 12 to reconstruct the most probable activity at the held-out location (red).

99 (Fig. 1A); for Dataset 2, this yielded clean recordings from 3159 electrodes from 24 patients.  
100 Each individual patient contributes electrodes from a limited set of brain locations, which we  
101 localized in a common space [MNI152; 10]; an example Dataset 1 patient’s 54 electrodes that  
102 passed the predefined kurtosis test are highlighted in black and red.

The recording from a given electrode is maximally informative about the activity of the neural tissue immediately surrounding its recording surface. However, brain regions that are distant from the recording surface of the electrode also contribute to the recording, albeit (*ceteris paribus*) to a much lesser extent. One mechanism underlying these contributions is volume conduction. The precise rate of falloff due to volume conduction (i.e., how much a small volume of brain tissue at location  $x$  contributes to the recording from an electrode at location  $\eta$ ) depends on the size of the recording surface, the electrode’s impedance, and the conductance profile of the volume of brain between  $x$  and  $\eta$ . As an approximation of this intuition, we place a Gaussian radial basis function (RBF) at the location  $\eta$  of each electrode’s recording surface (Fig. 1B). We use the values of the RBF at any brain location  $x$  as a rough estimate of how much structures around  $x$  contributed to the recording from location  $\eta$ :

$$\text{rbf}(x|\eta, \lambda) = \exp \left\{ -\frac{\|x - \eta\|^2}{\lambda} \right\}, \quad (1)$$

103 where the width variable  $\lambda$  is a parameter of the algorithm (which may in principle be set  
104 according to location-specific tissue conductance profiles) that governs the level of spatial  
105 smoothing. In choosing  $\lambda$  for the analyses presented here, we sought to maximize spatial  
106 resolution (which implies a small value of  $\lambda$ ) while also maximizing the algorithm’s ability  
107 to generalize to any location throughout the brain, including those without dense electrode  
108 coverage (which implies a large value of  $\lambda$ ). Here we set  $\lambda = 20$ , guided in part by our prior  
109 work [22, 24], and in part by examining the brain coverage with non-zero weights achieved by  
110 placing RBFs at each electrode location in Dataset 1 and taking the sum (across all electrodes)  
111 at each voxel in a  $4 \text{ mm}^3$  MNI brain. (We then held  $\lambda$  fixed for our analyses of Dataset 2.) We

<sup>112</sup> note that this value could in theory be further optimized, e.g., using cross validation or a formal  
<sup>113</sup> model [e.g., 24].

<sup>114</sup> A second mechanism whereby a given region  $x$  can contribute to the recording at  $\eta$  is  
<sup>115</sup> through (direct or indirect) anatomical connections between structures near  $x$  and  $\eta$ . We use  
<sup>116</sup> temporal correlations in the data to estimate these anatomical connections [2]. Let  $\bar{R}$  be the  
<sup>117</sup> set of locations at which we wish to estimate local field potentials, and let  $R_s \subseteq \bar{R}$  be set of  
<sup>118</sup> locations at which we observe local field potentials from patient  $s$  (excluding the electrodes that  
<sup>119</sup> did not pass the kurtosis test described above). In the analyses below we define  $\bar{R} = \cup_{s=1}^S R_s$ .  
<sup>120</sup> We can calculate the expected inter-electrode correlation matrix for patient  $s$ , where  $C_{s,k}(i, j)$  is  
<sup>121</sup> the correlation between the time series of voltages for electrodes  $i$  and  $j$  from subject  $s$  during  
<sup>122</sup> session  $k$ , using:

$$\bar{C}_s = r\left(\frac{1}{n}\left(\sum_{k=1}^n z(C_{s,k})\right)\right), \text{ where} \quad (2)$$

$$z(r) = \frac{\log(1+r) - \log(1-r)}{2} \text{ is the Fisher } z\text{-transformation and} \quad (3)$$

$$z^{-1}(z) = r(z) = \frac{\exp(2z) - 1}{\exp(2z) + 1} \text{ is its inverse.} \quad (4)$$

<sup>123</sup> Next, we use Equation 1 to construct a number of to-be-estimated locations by number of  
<sup>124</sup> patient electrode locations weight matrix,  $W_s$ . Specifically,  $W_s$  approximates how informative  
<sup>125</sup> the recordings at each location in  $R_s$  are in reconstructing activity at each location in  $\bar{R}$ , where  
<sup>126</sup> the contributions fall off with an RBF according to the distances between the corresponding  
<sup>127</sup> locations:

$$W_s(i, j) = \text{rbf}(i|j, \lambda). \quad (5)$$

<sup>128</sup> Given this weight matrix,  $W_s$ , and the observed inter-electrode correlation matrix for patient  
<sup>129</sup>  $s$ ,  $\bar{C}_s$ , we can estimate the correlation matrix for all locations in  $\bar{R}$  ( $\hat{C}_s$ ; Fig. 1C) using:

$$\hat{N}_s(x, y) = \sum_{i=1}^{|R_s|} \sum_{j=1}^{i-1} W(x, i) \cdot W(y, j) \cdot z(\bar{C}_s(i, j)) \quad (6)$$

$$\hat{D}_s(x, y) = \sum_{i=1}^{|R_s|} \sum_{j=1}^{i-1} W(x, i) \cdot W(y, j). \quad (7)$$

$$\hat{C}_s = r \left( \frac{\hat{N}_s}{\hat{D}_s} \right). \quad (8)$$

After estimating the numerator ( $\hat{N}_s$ ) and denominator ( $\hat{D}_s$ ) placeholders for each  $\hat{C}_s$ , we aggregate these estimates across the  $S$  patients to obtain a single expected full-brain correlation matrix ( $\hat{K}$ ; Fig. 1D):

$$\hat{K} = r \left( \frac{\sum_{s=1}^S \hat{N}_s}{\sum_{s=1}^S \hat{D}_s} \right). \quad (9)$$

Intuitively, the numerators capture the general structures of the patient-specific estimates of full-brain correlations, and the denominators account for which locations were near the implanted electrodes in each patient. To obtain  $\hat{K}$ , we compute a weighted average across the estimated patient-specific full-brain correlation matrices, where patients with observed electrodes near a particular set of locations in  $\hat{K}$  contribute more to the estimate.

Having used the multi-patient data to estimate a full-brain correlation matrix at the set of locations in  $\bar{R}$  that we wish to know about, we next use  $\hat{K}$  to estimate activity patterns everywhere in  $\bar{R}$ , given observations at only a subset of locations in  $\bar{R}$  (Fig. 1E).

Let  $\alpha_s$  be the set of indices of patient  $s$ 's electrode locations in  $\bar{R}$  (i.e., the locations in  $R_s$ ), and let  $\beta_s$  be the set of indices of all other locations in  $\bar{R}$ . In other words,  $\beta_s$  reflects the locations in  $\bar{R}$  where we did not observe a recording for patient  $s$  (these are the recording locations we will want to fill in using SuperEEG). We can sub-divide  $\hat{K}$  as follows:

$$\hat{K}_{\beta_s, \alpha_s} = \hat{K}(\beta_s, \alpha_s), \text{ and} \quad (10)$$

$$\hat{K}_{\alpha_s, \alpha_s} = \hat{K}(\alpha_s, \alpha_s). \quad (11)$$

142 Here  $\hat{K}_{\beta_s, \alpha_s}$  represents the correlations between the “unknown” activity at the locations in  $\beta_s$   
 143 and the observed activity at the locations in  $\alpha_s$ , and  $\hat{K}_{\alpha_s, \alpha_s}$  represents the correlations between  
 144 the observed recordings (at the locations in  $\alpha_s$ ).

145 Let  $Y_{s,k,\alpha_s}$  be the number-of-timepoints ( $T$ ) by  $|\alpha_s|$  matrix of (observed) voltages from the  
 146 electrodes in  $\alpha_s$  during session  $k$  from patient  $s$ . Then we can estimate the voltage from patient  
 147  $s$ ’s  $k^{th}$  session at the locations in  $\beta_s$  using [27]:

$$\hat{Y}_{s,k,\beta_s} = ((\hat{K}_{\beta_s, \alpha_s} \cdot \hat{K}_{\alpha_s, \alpha_s}^{-1}) \cdot Y_{s,k,\alpha_s}^T)^T. \quad (12)$$

148 This equation is the foundation of the SuperEEG algorithm. Whereas we observe recordings  
 149 only at the locations indexed by  $\alpha_s$ , Equation 12 allows us to estimate the recordings at all loca-  
 150 tions indexed by  $\beta_s$ , which we can define *a priori* to include any locations we wish, throughout  
 151 the brain. This yields estimates of the time-varying voltages at *every* location in  $\bar{R}$ , provided that  
 152 we define  $\bar{R}$  in advance to include the union of all of the locations in  $R_s$  and all of the locations  
 153 at which we wish to estimate recordings (i.e., a timeseries of voltages).

154 We designed our approach to be agnostic to electrode impedances, as electrodes that do not  
 155 exist do not have impedances. Therefore our algorithm recovers voltages in standard deviation  
 156 ( $z$ -scored) units rather than attempting to recover absolute voltages. (This property reflects  
 157 the fact that  $\hat{K}_{\beta_s, \alpha_s}$  and  $\hat{K}_{\alpha_s, \alpha_s}$  are correlation matrices rather than covariance matrices.) Also,  
 158 note that Equation 12 requires computing a  $T$  by  $T$  matrix, which can become computationally  
 159 intractable when  $T$  is very large (e.g., for the patient highlighted in Fig. 2,  $T = 12786750$ ).

<sup>160</sup> However, because Equation 12 is time invariant, we may compute  $Y_{s,k,\beta_s}$  in a piecewise manner  
<sup>161</sup> by filling in  $Y_{s,k,\beta_s}$  one row at a time (using the corresponding samples from  $Y_{s,k,\alpha_s}$ ).

<sup>162</sup> The SuperEEG algorithm described above and in Figure 1 allows us to estimate, up to a  
<sup>163</sup> constant scaling factor, local field potentials (LFPs) for each patient at all arbitrarily chosen  
<sup>164</sup> locations in the set  $\bar{R}$ , even if we did not record that patient's brain at all of those locations. We next  
<sup>165</sup> turn to an evaluation of the accuracy of those estimates.

## <sup>166</sup> Results

<sup>167</sup> We used a cross-validation approach to test the accuracy with which the SuperEEG algorithm  
<sup>168</sup> reconstructs activity throughout the brain. For each patient in turn, we estimated full-brain  
<sup>169</sup> correlation matrices (Eqn. 9) using data from all of the *other* patients. This step ensured that the  
<sup>170</sup> data we were reconstructing could not also be used to estimate the between-location correlations  
<sup>171</sup> that drove the reconstructions via Equation 12 (otherwise the analysis would be circular). For  
<sup>172</sup> that held-out patient, for each of their electrodes in turn, we used Equation 12 to reconstruct  
<sup>173</sup> activity at the held-out electrode location, using the correlation matrix learned from all other  
<sup>174</sup> patients' data as  $\hat{K}$ , and using activity recorded from the other electrodes from the held-out  
<sup>175</sup> patient as  $Y_{s,k,\alpha_s}$ . We then asked: how closely did each of the SuperEEG-estimated recordings  
<sup>176</sup> at those electrodes match the observed recordings from those electrodes (i.e., how closely did  
<sup>177</sup> the estimated  $\hat{Y}_{s,k,\beta_s}$  match the observed  $Y_{s,k,\beta_s}$ ?).

<sup>178</sup> To illustrate our approach, we first examine an individual held-out raw LFP trace and its  
<sup>179</sup> associated SuperEEG-derived reconstruction. Figure 2A displays the observed LFP from the red  
<sup>180</sup> electrode in Figure 1A (blue), and its associated reconstruction (red), during a 5 s time window  
<sup>181</sup> during one of the example patient's six recording sessions. The two traces match closely  
<sup>182</sup> ( $r = 0.86, p < 10^{-10}$ ). Figure 2B displays a two-dimensional histogram of the actual versus  
<sup>183</sup> reconstructed voltages for the entire 14.2 total hours of recordings from the example electrode

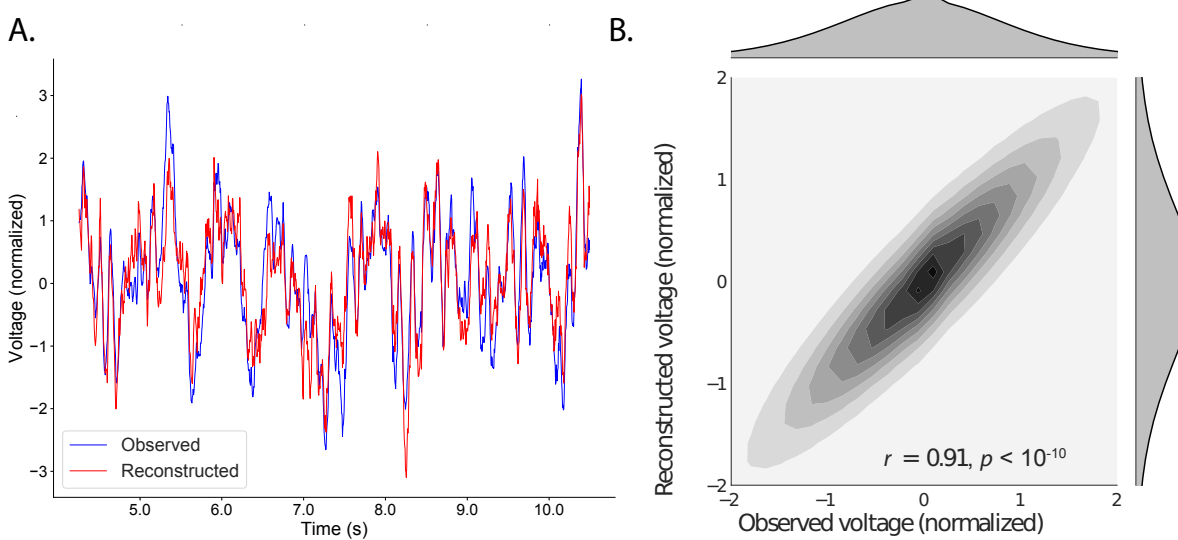


**Figure 2: Observed and reconstructed LFP from a single electrode.** **A. Example LFP.** A 5 s recording from the red electrode in Figure 1A is displayed in blue, and the reconstructed LFP during the same time window is shown in red. **B. Observed versus reconstructed LFP over 14.2 hours.** The two-dimensional histogram reflects the relation between distributions of observed versus reconstructed voltages from one patient, across the 14.2 hours of recorded data collected over 6 recording sessions. The correlation reported in the panel is between the observed and reconstructed voltages. Both panels: all voltages are represented in standard deviation units (computed within session).

(correlation:  $r = 0.91, p < 10^{-10}$ ). This example confirms that the SuperEEG algorithm recovers the recordings from this single electrode well. Next, we used this general approach to quantify the algorithm's performance across the full dataset.

For each held-out electrode, from each held-out patient in turn, we computed the average correlation (across recording sessions) between the SuperEEG-reconstructed voltage traces and the observed voltage traces from that electrode. For this analysis we set  $\bar{R}$  to be the union of all electrode locations across all patients. This yielded a single correlation coefficient for each electrode location in  $\bar{R}$ , reflecting how well the SuperEEG algorithm was able to recover the recording at that location by incorporating data across patients (black histogram in Fig. 3A, map in Fig. 3C). The observed distribution of correlations was centered well above zero (mean: 0.52;

<sup>194</sup>  $t$ -test comparing mean of distribution of  $z$ -transformed average patient correlation coefficients  
<sup>195</sup> to 0:  $t(66) = 25.08, p < 10^{-10}$ ), indicating that the SuperEEG algorithm recovers held-out  
<sup>196</sup> activity patterns substantially better than random guessing.

<sup>197</sup> As a stricter benchmark, we compared the quality of these across-participant reconstructions  
<sup>198</sup> (i.e., computed using a correlation model learned from other patients' data) to reconstructions  
<sup>199</sup> generated using a correlation model trained using the in-patient's data. In other words, for  
<sup>200</sup> this within-patient benchmark analysis we estimated  $\hat{C}_s$  (Eqn. 8) for each patient in turn, using  
<sup>201</sup> recordings from all of that patient's electrodes except at the location we were reconstructing.  
<sup>202</sup> These within-patient reconstructions serve as an estimate of how well data from all of the  
<sup>203</sup> other electrodes from that single patient may be used to estimate held-out data from the  
<sup>204</sup> same patient. This allows us to ask how much information about the activity at a given  
<sup>205</sup> electrode might be inferred through (a) volume conductance or other sources of "leakage"  
<sup>206</sup> from activity patterns measured from the patient's other electrodes and (b) across-electrode  
<sup>207</sup> correlations learned from that single patient. As shown in Figure 3A (gray histogram), the  
<sup>208</sup> distribution of within-patient correlations was centered well above zero (mean: 0.32;  $t$ -test  
<sup>209</sup> comparing mean of distribution of  $z$ -transformed average patient correlation coefficients to 0:  
<sup>210</sup>  $t(66) = 15.16, p < 10^{-10}$ ). However, the across-patient correlations were substantially higher  
<sup>211</sup> ( $t$ -test comparing average  $z$ -transformed within versus across patient electrode correlations:  
<sup>212</sup>  $t(66) = 9.62, p < 10^{-10}$ ). This is an especially conservative test, given that the across-patient  
<sup>213</sup> SuperEEG reconstructions exclude (from the correlation matrix estimates) all data from the  
<sup>214</sup> patient whose data is being reconstructed. We repeated each of these analyses on a second  
<sup>215</sup> independent dataset and found similar results (Fig. 3B, D; within versus across reconstruction  
<sup>216</sup> accuracy:  $t(23) = 6.93, p < 10^{-5}$ ). We also replicated this result separately for each of the two  
<sup>217</sup> experiments from Dataset 2 (Fig. S1). This overall finding, that reconstructions of held-out  
<sup>218</sup> data using correlation models learned from *other* patient's data yield higher reconstruction

accuracy than correlation models learned from the patient whose data is being reconstructed, has two important implications. First, it implies that distant electrodes provide additional predictive power to the data reconstructions beyond the information contained solely in nearby electrodes. (This follows from the fact that each patient’s electrodes are implanted in a unique set of locations, so for any given electrode the closest electrodes in the full dataset are likely to come from the same patient.) Second, it implies that the spatial correlations learned using the SuperEEG algorithm are, to some extent, similar across people.

The recordings we analyzed from Dataset 1 comprised data collected as the patients performed a variety of (largely idiosyncratic) tasks throughout each day’s recording session. That we observed reliable reconstruction accuracy across patients suggests that the spatial correlations derived from the SuperEEG algorithm are, to some extent, similar across tasks. We tested this finding more explicitly using Dataset 2. In Dataset 2, the recordings were limited to times when each patient was participating in each of two experiments (Experiment 1, a random-word list free recall task, and Experiment 2, a categorized list free recall task). We wondered whether a correlation model learned from data from one experiment might yield good predictions of data from the other experiment. Further, we wondered about the extent to which it might be beneficial or harmful to combine data across tasks.

To test the task-specificity of the SuperEEG-derived correlation models, we repeated the above within- and across-patient cross validation procedures separately for Experiment 1 and Experiment 2 data from Dataset 2. We then compared the reconstruction accuracies for held-out electrodes, for models trained within versus across the two experiments, or combining across both experiments (Fig. S2). In every case we found that across-patient models trained using data from all other patients out-performed within-patient models trained on data only from the subject contributing the given electrode ( $ts(24) > 6.50, ps < 10^{-5}$ ). All reconstruction accuracies also reliably exceeded chance performance ( $ts(24) > 8.00, ps < 10^{-8}$ ). Average reconstruction

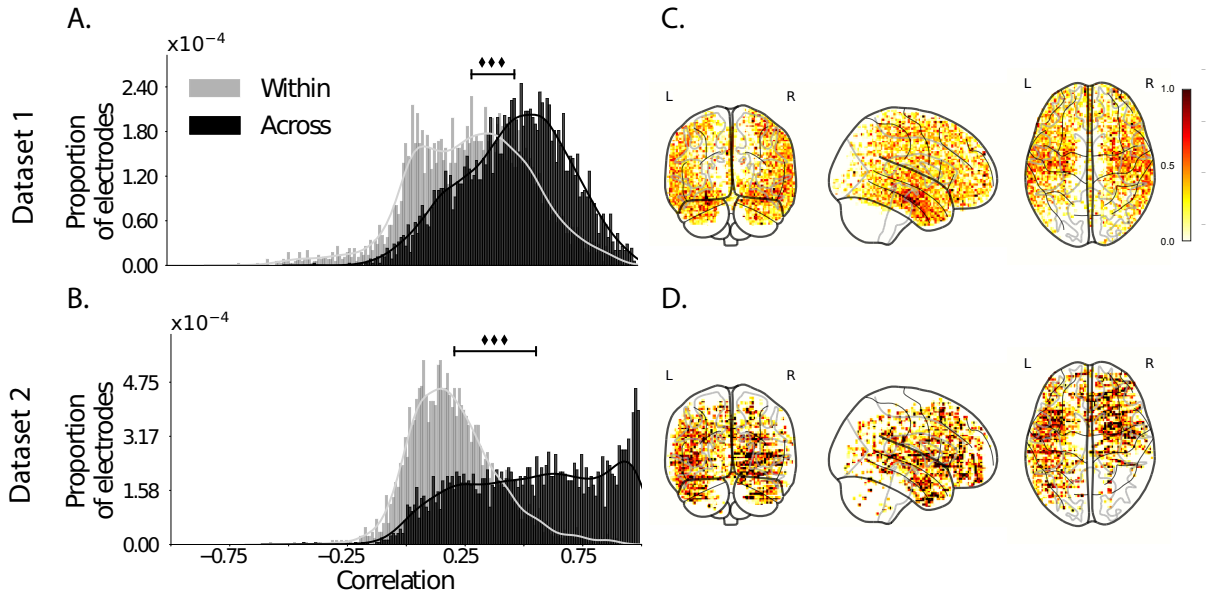


**Figure 3: Reconstruction quality across all electrodes in two ECoG datasets. A. Distributions of correlations between observed versus reconstructed activity by electrode, for Dataset 1.** The across-patient distribution (black) reflects reconstruction accuracy (correlation) using a correlation model learned from all but one patient's data, and then applied to that held-out patient's data. The within-patient distribution (gray) reflects performance using a correlation model learned from the same patient who contributed the to-be-reconstructed electrode. **B. Distributions of correlations for Dataset 2.** This panel is in the same format as Panel A, but reflects results obtained from Dataset 2. The histograms aggregate data across both Dataset 2 experiments; for results broken down by experiment see Figure S3. **C.–D. Reconstruction performance by location.** Each dot reflects the location of a single implanted electrode from Dataset 1 (Panel C) or Dataset 2 (Panel D). The dot colors denote the average across-session correlation, using the across-patient correlation model, between the observed and reconstructed activity at the given electrode location.

accuracy was highest for the across-patient models limited to data from the same experiment (mean accuracy: 0.68); next-highest for the across-patient models that combined data across both experiments (mean accuracy: 0.61); and lowest for models trained across task (mean accuracy: 0.47). This result also held for each of the Dataset 2 experiments individually (Fig. S3). Taken together, these results indicate that there are reliable commonalities in the spatial correlations of full-brain activity across tasks, but that there are also reliable differences in these spatial correlations across tasks. Whereas reconstruction accuracy benefits from incorporating data from other patients, reconstruction accuracy is highest when constrained to within-task data, or data that includes a variety of tasks (e.g., Dataset 1, or combining across the two Dataset 2 experiments).

Although both datasets we examined provide good full-brain coverage (when considering data from every patient; e.g. Fig. 3C, D), electrodes are not placed uniformly throughout the brain. For example, electrodes are more likely to be implanted in regions like the medial temporal lobe (MTL), and are rarely implanted in occipital cortex (Fig. 4A, B). Separately for each dataset, for each voxel in the  $4\text{ mm}^3$  voxel MNI152 brain, we computed the proportion of electrodes in the dataset that were contained within a 20 MNI unit radius sphere centered on that voxel. We defined the *density* at that location as this proportion. Across Datasets 1 and 2, the electrode placement densities were similar (correlation by voxel:  $r = 0.56, p < 10^{-10}$ ). We wondered whether regions with good coverage might be associated with better reconstruction accuracy (e.g. Fig. 3C, D indicate that many electrodes in the MTL have relatively high reconstruction accuracy, and occipital electrodes tend to have relatively low reconstruction accuracy). To test whether this held more generally across the entire brain, for each dataset we computed the electrode placement density for each electrode from each patient (using the proportion of *other* patients' electrodes within 20 MNI units of the given electrode). We then correlated these density values with the across-patient reconstruction accuracies for each

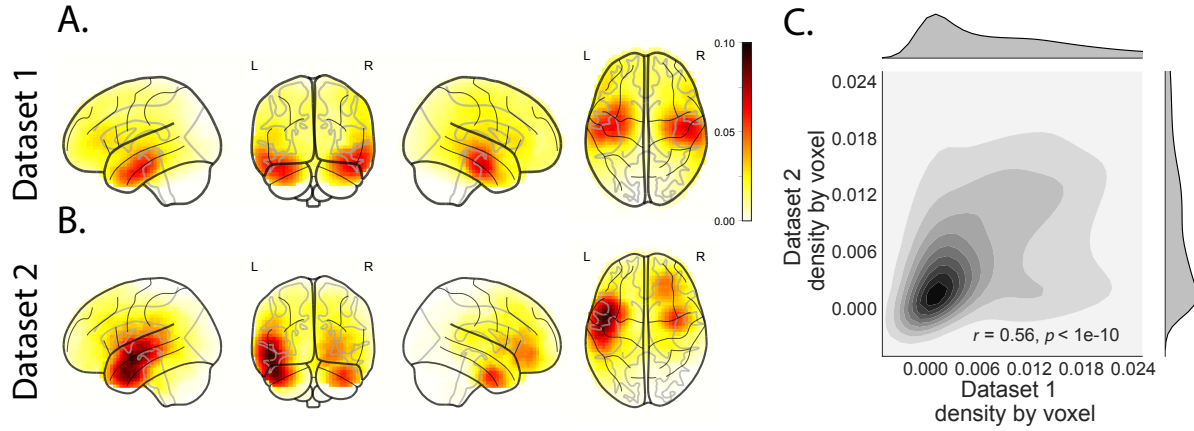


**Figure 4: Electrode sampling density by location.** **A. Electrode sampling density by voxel in Dataset 1.** Each voxel is colored by the proportion of total electrodes in the dataset that are located within a 20 MNI unit radius sphere centered on the given voxel. **B. Electrode sampling density by voxel in Dataset 2.** This panel displays the sampling density map for Dataset 2, in the same format as Panel A. **C. Correspondence in sampling density by voxel across Datasets 1 and 2.** The two-dimensional histogram displays the by-voxel densities in the two Datasets, and the one-dimensional histograms display the proportions of voxels in each dataset with the given density value. The correlation reported in the panel is across voxels in the  $4 \text{ mm}^3$  MNI brain.

269 electrode. Contrary to our expectation, rather than positive correlations, we found weak (but  
 270 reliable) negative correlations between reconstruction accuracy and density for both datasets  
 271 (Dataset 1:  $r = -0.07, p < 10^{-5}$ ; Dataset 2:  $r = -0.18, p < 10^{-10}$ ). This indicates that the  
 272 reconstruction accuracies we observed are not driven solely by sampling density, but rather  
 273 may also reflect higher order properties of neural dynamics such as functional correlations  
 274 between distant voxels [3].

275 In neurosurgical applications where one wishes to infer full-brain activity patterns, can our  
 276 framework yield insights into where the electrodes should be placed? A basic assumption of our  
 277 approach (and of most prior ECoG work) is that electrode recordings are most informative about  
 278 the neural activity near the recording surface of the electrode. But if we consider that activity  
 279 patterns throughout the brain are meaningfully correlated, are there particular implantation  
 280 locations that, if present in a patient's brain, yield especially high reconstruction accuracies

throughout the rest of the brain? For example, one might hypothesize that brain structures that are heavily interconnected with many other structures could be more informative about full-brain activity patterns than comparatively isolated structures.

To gain insights into whether particular electrode locations might be especially informative, we first computed the average reconstruction accuracy across all of each patient's electrodes (using the across-patients cross validation test; black histograms in Fig. 3A and B). We labeled each patient's electrodes in each dataset with the average reconstruction accuracy for that patient. In other words, we assigned every electrode from each given patient the same value, reflecting how well the activity patterns at those electrodes were reconstructed on average. Next, for each voxel in the 4 mm<sup>3</sup> MNI brain, we computed the average value across any electrode (from any patient) that came within 20 MNI units of that voxel's center. Effectively, we computed an *information score* for each voxel, reflecting the average reconstruction accuracy across any patients with electrodes near each voxel—where the averages were weighted to reflect patients who had more electrodes implanted near that location. This yielded a single map for each dataset, highlighting regions that are potentially promising implantation targets in terms of providing full-brain activity information via SuperEEG (Fig. 5A, B). Despite task and patient differences across the two datasets, we nonetheless found that the maps of the most promising implantation targets derived from both datasets were similar (voxelwise correlation between information scores across the two datasets:  $r = 0.03, p < 10^{-10}$ ). While the correspondence between the two maps was not perfect, our finding that there were some commonalities between the two maps lends support to the notion that different brain areas are differently informative about full-brain activity patterns. Further, we found the intersection of the top 10% of the most informative voxels between the two datasets (Fig. S5) and found gray matter regions like the right postcentral gyrus, right supramarginal gyrus, and the right nucleus accumbens that exhibited strong information scores in both datasets may be especially promising implantation

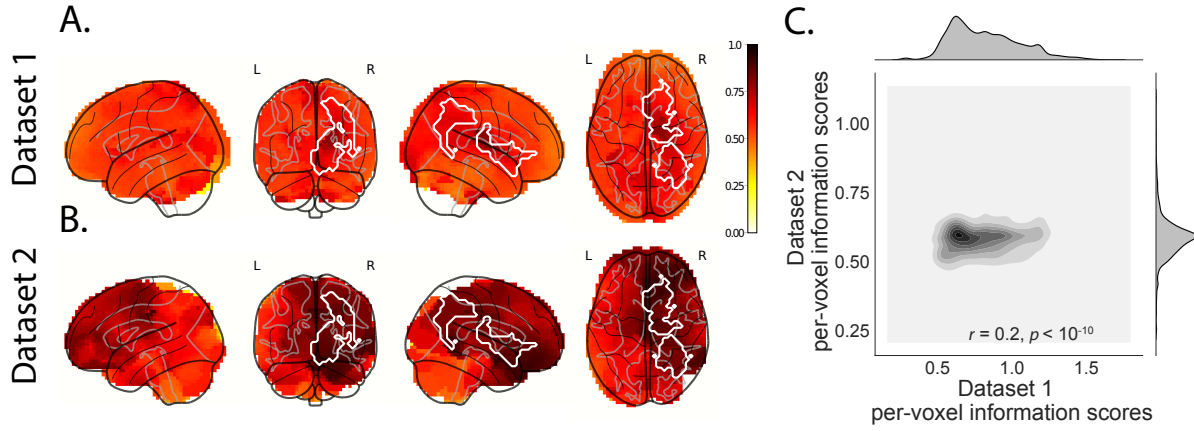


**Figure 5: Most informative electrode locations.** **A. Dataset 1 information score by voxel.** The voxel colors reflect the weighted average reconstruction accuracy across all electrodes from any patients with at least one electrode within 20 MNI units of the given voxel. **B. Dataset 2 information score by voxel.** This panel is in the same format as Panel A. In both panels the contours indicate the intersections between the top 10% most informative voxels in each map. **C. Correspondence in information scores by voxel across Datasets 1 and 2.** Same format as Figure 4C.

306 targets.

## 307 Discussion

308 Are our brain's networks static or dynamic? And to what extent are the network properties  
 309 of our brains stable across people and tasks? One body of work suggests that our brain's  
 310 *functional* networks are dynamic [e.g., 24], person-specific [e.g., 9], and task-specific [e.g.,  
 311 39]. In contrast, although the gross anatomical structure of our brains changes meaningfully  
 312 over the course of years as our brains develop, on the timescales of typical neuroimaging ex-  
 313 periments (i.e., hours to days) our anatomical networks are largely stable [e.g., 4]. Further,  
 314 many aspects of brain anatomy, including white matter structure, are largely preserved across  
 315 people [e.g., 15, 26, 37]. There are several possible means of reconciling this apparent inconsis-  
 316 tency between dynamic person- and task-specific functional networks versus stable anatomical  
 317 networks. For example, relatively small magnitude anatomical differences across people may

318 be reflected in reliable functional connectivity differences. Along these lines, one recent study  
319 found that diffusion tensor imaging (DTI) structural data is similar across people, but may be  
320 used to predict person-specific resting state functional connectivity data [2]. Similarly, other  
321 work indicates that task-specific functional connectivity may be predicted by resting state func-  
322 tional connectivity data [5, 38]. Another (potentially complementary) possibility is that our  
323 functional networks are constrained by anatomy, but nevertheless exhibit (potentially rapid)  
324 task-dependent changes [e.g., 36].

325 Here we have taken a model-based approach to studying whether high spatiotemporal  
326 resolution activity patterns throughout the human brain may be explained by a static connec-  
327 tome model that is shared across people and tasks. Specifically, we trained a model to take  
328 in recordings from a subset of brain locations, and then predicted activity patterns during the  
329 same interval, but at *other* locations that were held out from the model. Our model, based on  
330 Gaussian process regression, was built on three general hypotheses about the nature of the  
331 correlational structure of neural activity (each of which we tested). First, we hypothesized that  
332 functional correlations are stable over time and across tasks. We found that, although aspects  
333 of the patients’ functional correlations that were stable across tasks, we achieved better recon-  
334 struction accuracy when we trained the model on within-task data [we acknowledge that our  
335 general approach could potentially be extended to better model across-task changes, following  
336 5, 38, and others]. Second, we hypothesized that some of the correlational structure of peo-  
337 ple’s brain activity is similar across individuals. Consistent with this hypothesis, our model  
338 explained the data best when we trained the correlation model using data from *other* patients—  
339 even when compared to a correlation model trained on the same patient’s data. Third, we  
340 resolved ambiguities in the data by hypothesizing that neural activity from nearby sources will  
341 tend to be similar, all else being equal. This hypothesis was supported through our finding that  
342 all of the models we trained that incorporated this spatial smoothness assumption predicted

343 held-out data well above chance.

344 One potential limitation of our approach is that it does not provide a natural means of  
345 estimating the precise timing of single-neuron action potentials. Prior work has shown that  
346 gamma band and broadband activity in the LFP may be used to estimate the firing rates of  
347 neurons that underly the population contributing to the LFP [6, 14, 20, 25]. Because SuperEEG  
348 reconstructs LFPs throughout the brain, one could in principle use gamma or broadband power  
349 in the reconstructed signals to estimate the corresponding firing rates (though not the timings  
350 of individual action potentials).

351 Beyond providing a means of estimating ongoing activity throughout the brain using al-  
352 ready implanted electrodes, our work also has implications for where to place the electrodes in  
353 the first place. Electrodes are typically implanted to maximize coverage of suspected epilep-  
354 togenic tissue. However, our findings suggest that this approach could be further optimized.  
355 Specifically, one could leverage not only the non-invasive recordings taken during an initial  
356 monitoring period (as is currently done routinely), but also recordings collected from other  
357 patients. We could then ask: given what we learn from other patients' data (and potentially  
358 from the scalp EEG recordings of this new patient), where should we place a fixed number of  
359 electrodes to maximize our ability to map seizure foci? As shown in Figure 5, recordings from  
360 different locations are differently informative in terms of reconstructing the spatiotemporal  
361 activity patterns throughout the brain. This property might be leveraged in decisions about  
362 where to surgically implant electrodes in future patients.

363 **Concluding remarks**

364 Over the past several decades, neuroscientists have begun to leverage the strikingly profound  
365 mathematical structure underlying the brain's complexity to infer how our brains carry out  
366 computations to support our thoughts, actions, and physiological processes. Whereas tradi-

367 tional beamforming techniques rely on geometric source-localization of signals measured at the  
368 scalp, here we propose an alternative approach that leverages the rich correlational structure  
369 of two large datasets of human intracranial recordings. In doing so, we are one step closer to  
370 observing, and perhaps someday understanding, the full spatiotemporal structure of human  
371 neural activity.

## 372 **Code availability**

373 We have published an open-source toolbox implementing the SuperEEG algorithm. It may  
374 be downloaded [here](#). Additionally, we have provided notebooks for all analyses and figures  
375 reported here.

## 376 **Data availability**

377 The dataset analyzed in this study was generously shared by Michael Kahana. A portion of  
378 Dataset 1 may be downloaded [here](#). Dataset 2 may be downloaded [here](#).

## 379 **Acknowledgements**

380 We are grateful for useful discussions with Luke J. Chang, Uri Hasson, Josh Jacobs, Michael  
381 Kahana, and Matthijs van der Meer. We are also grateful to Michael Kahana for generously  
382 sharing the ECoG data we analyzed in our paper, which was collected under NIMH grant  
383 MH55687 and DARPA RAM Cooperative Agreement N66001-14-2-4-032, both to MJK. Our  
384 work was also supported in part by NSF EPSCoR Award Number 1632738 and by a sub-  
385 award of DARPA RAM Cooperative Agreement N66001-14-2-4-032 to JRM. The content is solely  
386 the responsibility of the authors and does not necessarily represent the official views of our  
387 supporting organizations.

388 **Author Contributions**

389 J.R.M conceived and initiated the project. L.L.W.O. and A.C.H. performed the analyses. J.R.M.  
390 and L.L.W.O. wrote the manuscript.

391 **Author Information**

392 Reprints and permissions information is available at [www.nature.com/reprints](http://www.nature.com/reprints). The authors  
393 declare no competing financial interests. Readers are welcome to comment on the online  
394 version of the paper. Publisher's note: Springer Nature remains neutral with regard to jurisdic-  
395 tional claims in published maps and institutional affiliations. Correspondence and requests for  
396 materials should be addressed to J.R.M. ([jeremy.r.manning@dartmouth.edu](mailto:jeremy.r.manning@dartmouth.edu)).

397 **References**

- 398 [1] Baillet, S., Mosher, J. C., and Leahy, R. M. (2001). Electromagnetic brain mapping. *IEEE*  
399 *Signal Processing Magazine*, 18:14–30.
- 400 [2] Becker, C. O., Pequito, S., Pappas, G. J., Miller, M. B., adn D S Bassett, S. T. G., and Preciado,  
401 V. M. (2018). Spectral mapping of brain functional connectivity from diffusion imaging.  
402 *Scientific Reports*, 8(1411):<https://doi.org/10.1038/s41598-017-18769-x>.
- 403 [3] Betzel, R. F., Medaglia, J. D., Kahn, A. E., Soffer, J., Schonhaut, D. R., and Bassett, D. S.  
404 (2017). Inter-regional ecog correlations predicted by communication dynamics, geometry,  
405 and correlated gene expression. *arXiv*, page 1706.06088.
- 406 [4] Casey, B. J., Giedd, J. N., and Thomas, K. M. (2000). Structural and functional brain devel-  
407 opment and its relation to cognitive development. *Biological Psychology*, 54(1–3):241–257.
- 408 [5] Cole, M. W., Ito, T., Bassett, D. S., and Schultz, D. H. (2016). Activity flow over resting-state  
409 networks shapes cognitive task activations. *Nature Neuroscience*, 19(12):1718–1726.

- 410 [6] Crone, N. E., Korzeniewska, A., and Franaszczuk, P. (2011). Cortical gamma responses:  
411 searching high and low. *International Journal of Psychophysiology*, 79(1):9–15.
- 412 [7] Ezzyat, Y., Kragel, J. E., Burke, J. F., Levy, D. F., Lyalenko, A., Wanda, P., O’Sullivan, L.,  
413 Hurley, K. B., Busygin, S., Pedisich, I., Sperling, M. R., Worrell, G. A., Kucewicz, M. T., Davis,  
414 K. A., Lucas, T. H., Inman, C. S., Lega, B. C., Jobst, B. C., Sheth, S. A., Zaghloul, K., Jutras,  
415 M. J., Stein, J. M., Das, S. R., Gorniak, R., Rizzuto, D. S., and Kahana, M. J. (2017). Direct  
416 brain stimulation modulates encoding states and memory performance in humans. *Current  
417 Biology*, 27:1–8.
- 418 [8] Ezzyat, Y., Wanda, P. A., Levy, D. F., Kadel, A., Aka, A., Pedisich, I., Sperling, M. R.,  
419 Sharan, A. D., Lega, B. C., Burks, A., Gross, R. E., Inman, C. S., Jobst, B. C., Goren-  
420 stein, M. A., Davis, K. A., Worrell, G. A., Kucewicz, M. T., Stein, J. M., Gorniak, R.,  
421 Das, S. R., Rizzuto, D. S., and Kahana, M. J. (2018). Closed-loop stimulation of tem-  
422 poral cortex rescues functional networks and improves memory. *Nature Communications*,  
423 9(365):<https://doi.org/10.1038/s41467-017-02753-0>.
- 424 [9] Finn, E. S., Shen, X., Scheinost, D., Rosenberg, M. D., Huang, J., Chun, M. M., Papademetris,  
425 X., and Constable, R. T. (2015). Functional connectome fingerprinting: identifying individuals  
426 using patterns of brain connectivity. *Nature Neuroscience*, 18:1664 – 1671.
- 427 [10] Grabner, G., Janke, A. L., Budge, M. M., Smith, D., Pruessner, J., and Collins, D. L. (2006).  
428 Symmetric atlasing and model based segmentation: an application to the hippocampus in  
429 older adults. *Medical Image Computing and Computer-Assistend Intervention*, 9:58–66.
- 430 [11] Hillebrand, A., Singh, K. D., Holliday, I. E., Furlong, P. L., and Barnes, G. R. (2005). A new  
431 approach to neuroimaging with magnetoencephalography. *Human Brain Mapping*, 25:199–  
432 211.

- 433 [12] Horak, P. C., Meisenhelter, S., Song, Y., Testorf, M. E., Kahana, M. J., Viles, W. D., Bujarski,  
434 K. A., Connolly, A. C., Robbins, A. A., Sperling, M. R., Sharan, A. D., Worrell, G. A., Miller,  
435 L. R., Gross, R. E., Davis, K. A., Roberts, D. W., Lega, B., Sheth, S. A., Zaghloul, K. A., Stein,  
436 J. M., Das, S. R., Rizzuto, D. S., and Jobst, B. C. (2017). Interictal epileptiform discharges  
437 impair word recall in multiple brain areas. *Epilepsia*, 58(3):373–380.
- 438 [13] Huster, R. J., Debener, S., Eichele, T., and Herrmann, C. S. (2012). Methods for simultaneous  
439 EEG-fMRI: an introductory review. *The Journal of Neuroscience*, 32(18):6053–6060.
- 440 [14] Jacobs, J., Kahana, M. J., Ekstrom, A. D., Mollison, M. V., and Fried, I. (2010). A sense of  
441 direction in human entorhinal cortex. *Proceedings of the National Academy of Sciences, USA*,  
442 107(14):6487–6482.
- 443 [15] Jahanshad, N., Kochunov, P. V., Sprooten, E., Mandl, R. C., Nichols, T. E., Almasy, L.,  
444 Blangero, J., Brouwer, R. M., Curran, J. E., de Zubicaray, G. I., Duggirala, R., Fox, P. T., Hong,  
445 L. E., Landman, B. A., Martin, N. G., McMahon, K. L., Medland, S. E., Mitchell, B. D., Olvera,  
446 R. L., Peterson, C. P., Starr, J. M., Sussmann, J. E., Toga, A. W., Wardlaw, J. M., Wright, M. J.,  
447 Pol, H. E. H., Pastin, M. E., McIntosh, A. M., Deary, I. J., Thompson, P. M., and Glahn, D. C.  
448 (2013). Multi-site genetic analysis of diffusion images and voxelwise heritability analysis: A  
449 pilot project of the enigma-dti working group. *NeuroImage*, 81(1):455–469.
- 450 [16] Kragel, J. E., Ezzyat, Y., Sperling, M. R., Gorniak, R., Worrell, G. A., Berry, B. M., Inman,  
451 C., Lin, J.-J., Davis, K. A., Das, S. R., Stein, J. M., Jobst, B. C., Zaghloul, K. A., Sheth, S. A.,  
452 Rizzuto, D. S., and Kahana, M. J. (2017). Similar patterns of neural activity predict memory  
453 formation during encoding and retrieval. *NeuroImage*, 155:70–71.
- 454 [17] Kucewicz, M. T., Berry, B. M., Kremen, V., Brinkmann, B. H., Sperling, M. R., Jobst, B. C.,  
455 Gross, R. E., Lega, B., Sheth, S. A., Stein, J. M., Das, S. R., Gorniak, R., Stead, S. M., Rizzuto,

- 456 D. S., Kahana, M. J., and Worrell, G. A. (2017). Dissecting gamma frequency actiivty during  
457 human memory processing. *Brain*, 140:1337–1350.
- 458 [18] Kucewicz, M. T., Berry, B. M., Miller, L. R., Khadjevand, F., Ezzyat, Y., Stein, J. M., Kremen,  
459 V., Brinkmann, B. H., Wanda, P., Sperling, M. R., Gorniak, R., Davis, K. A., Jobst, B. C., Gross,  
460 R. E., Lega, B., Gompel, J. V., Stead, S. M., Rizzuto, D. S., Kahana, M. J., and Worrell, G. A.  
461 (2018). Evidence for verbal memory enhancement with electrical brain stimulation in the  
462 lateral temporal cortex. *Brain*, 141(4):971–978.
- 463 [19] Lin, J.-J., Rugg, M. D., Das, S., Stein, J., Rizzuto, D. S., Kahana, M. J., and Lega, B. C.  
464 (2017). Theta band power increases in the posterior hippocampus predict successful episodic  
465 memory encoding in humans. *Hippocampus*, 27:1040–1053.
- 466 [20] Manning, J. R., Jacobs, J., Fried, I., and Kahana, M. J. (2009). Broadband shifts in LFP power  
467 spectra are correlated with single-neuron spiking in humans. *The Journal of Neuroscience*,  
468 29(43):13613–13620.
- 469 [21] Manning, J. R., Polyn, S. M., Baltuch, G., Litt, B., and Kahana, M. J. (2011). Oscillatory  
470 patterns in temporal lobe reveal context reinstatement during memory search. *Proceedings of  
471 the National Academy of Sciences, USA*, 108(31):12893–12897.
- 472 [22] Manning, J. R., Ranganath, R., Norman, K. A., and Blei, D. M. (2014). Topographic  
473 factor analysis: a Bayesian model for inferring brain networks from neural data. *PLoS One*,  
474 9(5):e94914.
- 475 [23] Manning, J. R., Sperling, M. R., Sharan, A., Rosenberg, E. A., and Kahana, M. J. (2012).  
476 Spontaneously reactivated patterns in frontal and temporal lobe predict semantic clustering  
477 during memory search. *The Journal of Neuroscience*, 32(26):8871–8878.

- 478 [24] Manning, J. R., Zhu, X., Willke, T. L., Ranganath, R., Stachenfeld, K., Hasson, U., Blei,  
479 D. M., and Norman, K. A. (2018). A probabilistic approach to discovering dynamic full-brain  
480 functional connectivity patterns. *NeuroImage*.
- 481 [25] Miller, K. J., Shenoy, P., den Nijs, M., Sorensen, L. B., Rao, R. P. N., and Ojemann, J. G. (2008).  
482 Beyond the gamma band: the role of high-frequency features in movement classification.  
483 *IEEE Transactions on Biomedical Engineering*, 55(5):1634 – 1637.
- 484 [26] Mori, S., Oishi, K., Jiang, H., Jiang, L., Li, X., Akhter, K., Hua, K., Faria, A. V., Mahmood,  
485 A., Woods, R., Toga, A. W., Pike, G. B., Neto, P. R., Evans, A., Zhang, J., Huang, H., Miller,  
486 M. I., van Zijl, P., and Mazziotta, J. (2008). Stereotaxic white matter atlas based on diffusion  
487 tensor imaging in an icbm template. *NeuroImage*, 40(2):570–582.
- 488 [27] Rasmussen, C. E. (2006). *Gaussian processes for machine learning*. MIT Press.
- 489 [28] Sarvas, J. (1987). Basic mathematical and electromagnetic concepts of the biomagnetic  
490 inverse problem. *Phys. Med. Biol.*, 32(1):11–22.
- 491 [29] Sawyer, R. J. (1995). *The Terminal Experiment*. HarperPrism.
- 492 [30] Sederberg, P. B., Kahana, M. J., Howard, M. W., Donner, E. J., and Madsen, J. R. (2003). Theta  
493 and gamma oscillations during encoding predict subsequent recall. *Journal of Neuroscience*,  
494 23(34):10809–10814.
- 495 [31] Sederberg, P. B., Schulze-Bonhage, A., Madsen, J. R., Bromfield, E. B., Litt, B., Brandt,  
496 A., and Kahana, M. J. (2007a). Gamma oscillations distinguish true from false memories.  
497 *Psychological Science*, 18(11):927–932.
- 498 [32] Sederberg, P. B., Schulze-Bonhage, A., Madsen, J. R., Bromfield, E. B., McCarthy, D. C.,  
499 Brandt, A., Tully, M. S., and Kahana, M. J. (2007b). Hippocampal and neocortical gamma  
500 oscillations predict memory formation in humans. *Cerebral Cortex*, 17(5):1190–1196.

- 501 [33] Sejnowski, T. J., Churchland, P. S., and Movshon, J. A. (2014). Putting big data to good use  
502 in neuroscience. *Nature Neuroscience*, 17:1440–1441.
- 503 [34] Snyder, A. Z. (1991). Dipole source localization in the study of EP generators: a critique.  
504 *Electroencephalography and Clinical Neurophysiology*, 80(4):321–325.
- 505 [35] Solomon, E. A., Gross, R., Lega, B., Sperling, M. R., Worrell, G., Sheth, S. A., Zaghloul,  
506 K. A., Jobst, B. C., Stein, J. M., Das, S., Gorniak, R., Inman, C., Seger, S., Kragel, J. E., Rizzuto,  
507 D. S., and Kahana, M. J. (2018). Mtl functional connectivity predicts stimulation-induced  
508 theta power. *Nature Communications*, In press.
- 509 [36] Sporns, O. and Betzel, R. F. (2016). Modular brain networks. *Annual Review of Psychology*,  
510 67:613–640.
- 511 [37] Talairach, J. and Tournoux, P. (1988). *Co-planar stereotaxic atlas of the human brain*. Verlag,  
512 Stuttgart.
- 513 [38] Tavor, I., Jones, O. P., Mars, R. B., Smith, S. M., Behrens, T. E., and Jbabdi, S. (2016). Task-  
514 free MRI predicts individual differences in brain activity during task performance. *Science*,  
515 352(6282):216–220.
- 516 [39] Turk-Browne, N. B. (2013). Functional interactions as big data in the human brain. *Science*,  
517 342:580–584.
- 518 [40] Weidemann, C. T., Kragel, J. E., Lega, B. C., Worrell, G. A., Sperling, M. R., Sharan, A. D.,  
519 Jobst, B. C., Khadjevand, F., Davis, K. A., Wanda, P. A., Kadel, A., Rizzuto, D. S., and Kahana,  
520 M. J. (2018). Neural activity reveals interactions between episodic and semantic memory  
521 systems during retrieval. *Journal of Experimental Psychology: General*, In press.
- 522 [41] Yeo, B. T. T., Krienen, F. M., Sepulcre, J., Sabuncu, M. R., Lashkari, D., Hollinshead, M.,  
523 Roffman, J. L., Smoller, J. W., Zollei, L., Polimieni, J. R., Fischl, B., Liu, H., and Buckner,

- 524 R. L. (2011). The organization of the human cerebral cortex estimated by intrinsic functional  
525 connectivity. *Journal of Neurophysiology*, 106(3):1125–1165.